© JUL 2026 | IRE Journals | Volume 10 Issue 1 | ISSN: 2456-8880
DOI: https://doi.org/10.64388/ire1724954

Structural, Magnetic and Thermal Studies of Hydrothermally Synthesized Ni-Doped $BiFeO_3$ Nanoparticles

T. Firoz Khan[1], S. Devendra[1], D. Chandra Sekhar[1], J. Chandra Sekhar[2], K. Sreelekha[1]
[1] Lecturer in Physics, Department of Physics, Government College (Autonomous), Anantapur, Andhra Pradesh, India
[2] Lecturer in Physics, Department of Physics, SCNR Government Degree College, Proddatur, YSR Kadapa, Andhra Pradesh, India

Abstract- ***Ni-doped bismuth ferrite ($Bi_{1-x}Ni_xFeO_3$, x = 0.2–0.8) nanoparticles were successfully synthesized by the hydrothermal method and investigated systematically to understand the influence of Ni^{2+} substitution on their structural, magnetic, and thermal properties. The structural characteristics of the prepared nanoparticles were examined using X-ray diffraction (XRD), field-emission scanning electron microscopy (FESEM), and high-resolution transmission electron microscopy (HRTEM). XRD analysis confirmed the formation of a crystalline $BiFeO_3$-based phase, with systematic variations in lattice parameters and crystallite size resulting from Ni^{2+} incorporation into the $BiFeO_3$ lattice. The observed changes in structural parameters indicate lattice distortion associated with the substitution of Ni^{2+} ions. FESEM and HRTEM analyses revealed nanoscale grains with relatively homogeneous morphology.***

The magnetic properties were evaluated from room-temperature magnetization by vibration sample magnetometer (VSM). Ni substitution significantly modified the magnetic response of $BiFeO_3$ nanoparticles, with saturation magnetization values varying with Ni concentration. The enhanced magnetic behaviour is attributed to the modification of Fe–O–Fe super exchange interactions, spin canting, and disruption of the intrinsic cycloidal spin structure of $BiFeO_3$. Thermal behaviour was investigated using Thermo-Gravimetric analysis and Differential Scanning Calorimetry (TG–DSC), which revealed characteristic stages of mass loss and thermal transitions associated with dehydration, decomposition of precursor residues, crystallization, and formation of the stable oxide phase. The combined structural, magnetic, and thermal results demonstrate that Ni incorporation is an effective approach for tailoring the multifunctional properties of $BiFeO_3$ nanoparticles, making them promising candidates for potential applications in magnetic, spintronic, and multifunctional nano electronic devices.

Index Terms- ***$BiFeO_3$, FESEM, HRTEM, Hydrothermal synthesis, Nanoparticles, Ni doping, TG–DSC, VSM, X-ray diffraction***

I. INTRODUCTION

Perovskite materials received much attention in science and technology due to their peculiar properties like dielectric, ferroelectric, photocatalytic, nanocatalytic, piezoelectric, pyroelectric, etc., [1]. All these properties led the perovskites to achieve the applications in the charge stored capacitors, ferroelectric memory devices, piezo-sensors, solar cells (SCs)/photovoltaic devices, optoelectronic devices, and so on [2]. It is a familiar fact that the perovskite reveals an ABO3 chemical structure, wherein, the 'A' corresponds to divalent/trivalent elements, and the 'B' refers to the trivalent/tetravalent element [3]. Further, it is also noticed that some of the perovskites exhibited magnetic, dielectric, ferroelectric, and ferroelastic nature. Such systems are considered as multiferroic perovskites [4]. Among these multiferroics, the well familiar system is BiFeO3 [BF]. It showed good attention due to the applications such as spintronics, memory, energy storage, energy conversion, sensors, actuators, medical (like CT scan), catalysis, photonic devices, optoelectronics, tunnel junctions, etc., [5–6]. A significant research work is done on bismuth ferrite materials for several applications. In this regard, Visakh et al. [7], addressed the synthesis, and various characterizations of multiferroic nanocomposites revealing several applications. Celis et al. [8], introduced different mechanisms in order to control the multiferroic properties of BF nanoparticles. Indriyani et al. [9], fabricated the BF nanoparticles via one-pot method through abelmoschus esculentus leaves, and showed the photocatalytic dye degradation activity [10]. Basith et al. [11], synthesized the BF nanoparticles at low operating temperatures, and confirmed the high magnetization, photocatalytic dye degradation, and hydrogen evolution. Bai et al. [12], introduced various approaches for growing the BF crystals. Mocherla et al. [13], reported bandgap which was tunable in BF nanoparticles, and explained the role of microstrain, and defects. Prince et al. [14], developed the tuning of a few properties of BF such as structure, optical, and magnetism via the annealing. Masoudpanah et al. [15], synthesized the BF nanoparticles, and illustrated the structure, magnetic nature, and photocatalytic activity.

Besides, doping is performed extensively on BF nanoparticles for different applications. In view of this, Othman et al. [16], synthesized, and studied the structure, magnetic, and electric properties of Co-

doped BF nanoparticles. Shrimali et al. [17] studied the influence of magnetic field on dielectric properties of Co substituted BF nanoparticles and confirmed the magnetoelectric nature of samples. Gu et al. [18], fabricated BiSmFeO3 particles and evidenced magnetic nature by studying the magnetic properties. Also, the optical properties are investigated around the morphotropic phase boundary. Banu et al. [19], developed the BiNdNiFeO3 nanoparticles, and suggested for spintronic applications thereby showing the dopant effect. Sarkar et al. [20], offered a clear picture on the differences between the undoped, and Ni-doped BF nanoparticles (prepared via solution combustion route) in terms of structure, electronic behaviour, and magnetic nature. This detailed literature survey ensured that the research work is done on Ni-doped BF nanoparticles. But the methodology is different for different samples. That is, it manifests that the solution and alloying techniques like chemical route, combustion method, sol-gel, ball milling etc., are used to synthesize the samples. But the hydrothermal method was not opted, which is considered as a technique that brings lots of changes in microstructure and further inducing the changes in other dependent properties.

Moreover, the properties were not studied collectively in a single literature paper providing the difference and connectivity of all properties. Therefore, in the current work, authors focused on synthesizing $Bi_{1-x}Ni_xFeO_3$ (x = 0.20 – 0.80) (BNF) nanoparticles using hydrothermal method at low operating temperatures (100 °C–150 °C). Upon preparing the BNF nanoparticles, the samples are intended to investigate the structure, morphology, nanoparticle confirmation, optical bandgap, functional groups/metal oxide bonds, magnetic and thermal behaviour, etc.

II. SYNTHESIS METHOD AND CHARACTERIZATION

At the outset, for the synthesis of $Bi_{1-x}Ni_xFeO_3$ nanoparticles (x = 0.2 – 0.8), initial precursor materials such as [$Bi(NO_3)_3.5H_2O$, ≥ 99.99% purity, Sigma-Aldrich], Nickel (II) nitrate hexahydrate [$Ni(NO_3)_2.6H_2O$, 99.92% purity, Sigma-Aldrich], and Iron (III) nitrate nonahydrate [$Fe(NO_3)_3.9H_2O$, 99.99% purity, Sigma-Aldrich] were considered. In addition, the NaOH pellets were taken which acts as the mineralizer, stabilizing the pH, facilitator for dissolving the materials, precipitation of reactants etc., during the BNF crystal grow th process. As a whole, the reaction kinetics will be influenced by NaOH solution. The preparation of BNF nanoparticles is similar to the method provided in the literature [21,22].

A step wise procedure for the synthesis is depicted in Figure 1. The precursors were first dissolved and stirred for 2 h to obtain a pleasant BNF solution. The NaOH solution was poured into it during the stirring process. Therefore, the reactive atmosphere among the participants gets developed in the BNF solution. From this solution BNF nanoparticles were prepared using autoclave process and centrifuged to remove the water content. After the centrifugation process, the remaining sample is heated at 50 °C for 2 h to expel the moisture from the nanoparticles. The powder obtained in such a way was grinded well using agate mortars and made into pellets using hydraulic press by applying the pressure ranging from 2 tons. The resultant powder, and pellets are characterized using the X-ray diffractometer (Bruker XRD, wavelength of CuKα = 0.15406 nm), Field-emission scanning electron microscopy (Ultra 55 FE-SEM, Carl Zeiss), Transmission electron microscopy (TEM, Model JEOL JEM 2100), Vibration Sample Magnetometry and Thermo-Gravimetric analysis and Differential Scanning Calorimetry (TG–DSC) for studying the structure, microstructure, metal oxide bonds, Magnetic behaviour etc., of BNF nanoparticles.

© JUL 2026 | IRE Journals | Volume 10 Issue 1 | ISSN: 2456-8880
DOI: https://doi.org/10.64388/ire1724954

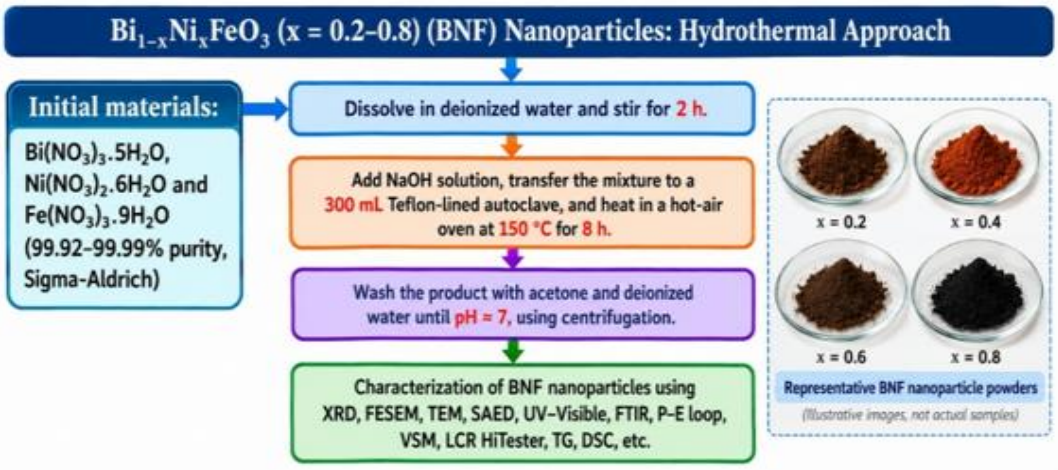


Fig.1 The schematic diagram for the synthesis of BNF nanoparticles

III. RESULT AND ANALYSIS

A. X-Ray Diffraction Analysis

The X-ray diffraction (XRD) patterns of the synthesized nanoparticles with different compositions (x = 0.2, 0.4, 0.6, and 0.8) were recorded over a (2θ) range of 10°–80° to investigate their structural characteristics and phase formation as shown in Fig.2. The diffraction peaks indicate the crystalline nature of the prepared samples, with prominent reflections observed around (2θ approximately 30°). The variations in peak intensity and profile with composition suggest changes in crystallinity and structural ordering. The major diffraction peaks are indexed to the characteristic crystallographic planes of $BiFeO_3$, including (012), (104), (110), (006), (202), and other higher-angle reflections. The x = 0.2, 0.6 & 0.8 samples show the high crystallinity pertaining the (104), and (110) reflection planes. The x = 0.4 reveals the same consisting of the low intensity. In this, the XRD patterns, the intensity is depending on the number of crystallites undergoing diffraction when compared to the CuKα (0.15406 nm) wavelength. The maximum intense peak is expressing the slit behaviour. Owing to the presence of trivalent element, the microstrain get developed leading to the peak slitting behaviour pertaining to the second reflection plane. The similar kind of trend is noticed in the literature [23]. According to Shannon ionic radii information [24], it is confirmed that the cations involved in the BNF system express the ionic radii as Bi^{3+}: 0.096 nm, Ni^{2+}: 0.072 nm, Fe^{3+}: 0.064 nm & Fe^{2+}: 0.063 nm. It is evident from this data that the upon doping the Ni into the perovskite BF system, the Ni^{2+} cations cannot occupy the Bi-position due to two factors. One is the huge ionic radii difference (25 % variation) which can develop the fluctuation of the site having unstable structure and the other one is, valency mismatch (+3 & +2). Therefore, the probable occupancy goes to ferric ions (Fe^{3+}). The reason is that the ionic radii of ferric, and nickel cations is having small variation, and hence, the chances are very high to occupy the ferric ion site by the nickel ions.

practically, it is seen in the Table.1. The lattice parameters demonstrate that the BNF structure is of rhombohedral as an inclusive of few secondary phases related to the $Bi_2Fe_4O_9$ (indexed by * symbol) (JCPDS file No:25-0090). The formation of secondary phase is a common phenomenon in the case of multiferroic perovskites pertaining the trivalent element as one of the elements as reported by Nadeem et al. [25]. The primary phases are on par with the BF reflection planes as indicated in the JCPDS file no:71-2494. The lattice constants, and unit cell volume parameters of BNF nanoparticles are determined using the unit cell software and listed in Table 1. The values are found to be increasing from 5.571-5.581 Å (a = b), and 13.875 - 13.882 Å (c) as a function of Ni-content. The unit cell volume (V) is found to be increasing in a minute manner ranging from 372.92 $Å^3$to 374.45 $Å^3$. The crystallite size (D) of BNF is calculated using the Scherrer equation:

$$D = \frac{0.9\lambda}{\beta \mathrm{Cos}\theta}$$

where 'β' - full width half maxima,

λ is the wavelength of CuKα (0.15416 nm) and

θ is the diffraction angle.

The crystallite size is found for individual peaks, and at the end the average values is taken into an account. This offers the average crystallite size as listed in Table.2. The results conveyed that the D-

© JUL 2026 | IRE Journals | Volume 10 Issue 1 | ISSN: 2456-8880
DOI: https://doi.org/10.64388/ire1724954

value is not varying monotonically (45.5, 58.2, 52.9 & 69.1 nm). However, it reveals the inversely proportional relationship with the variation of full width half maxima (FWHM, β: 0.781, 0.686, 0.720 & 0.485) with increase in 'x'.

The X-ray density of x = 0.2 - 0.8 is carried out using the equation

$$\rho_t = \frac{(Z * CMW)}{(N * V)}$$

where Z = effective number of atoms per unit cell for trigonal structure,

CMW is the compositional molecular weight, and

N is the Avogadro's number

The values are observed to be decreasing from 8.932 to 5.697 g/c.c., as a function of 'x'. This can be ascertained by the decreasing trend of compositional molecular weight from 250.77 to 160.60 drastically. The relationship variation implied a fact that the huge decrement is seen at high concentration of Ni. The trend of the obtained results almost follows the similar trend as reported in the literature [26-27].

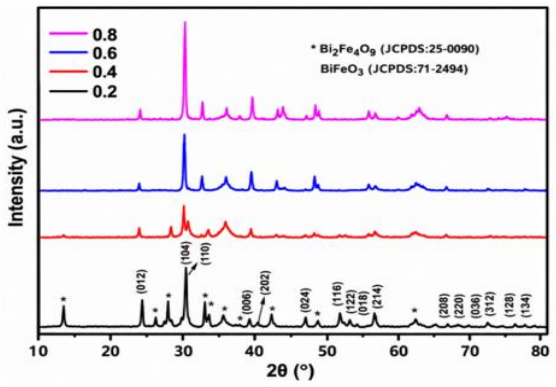


Fig.2 The XRD patterns of $Bi_{1-x}Ni_xFeO_3$ (x = 0.2 - 0.8) nanoparticles

Table.1 Structure and physical parameters of BNF nanoparticles

x	0.2	0.4	0.6	0.8
D (nm)	45.5 + 0.624	58.2 + 0.841	52.9 + 0.794	69.1 + 0.386
a = b (Å)	5.571	5.576	5.579	5.581
c (Å)	13.875	13.878	13.880	13.882
FWHM (β)	0.781	0.686	0.720	0.485
V ($Å^3$)	372.92	373.67	374.13	374.45
CMW (g/mole)	250.77	220.71	190.65	160.60
ρ_t (g/c.c.)	8.932	7.845	6.769	5.697

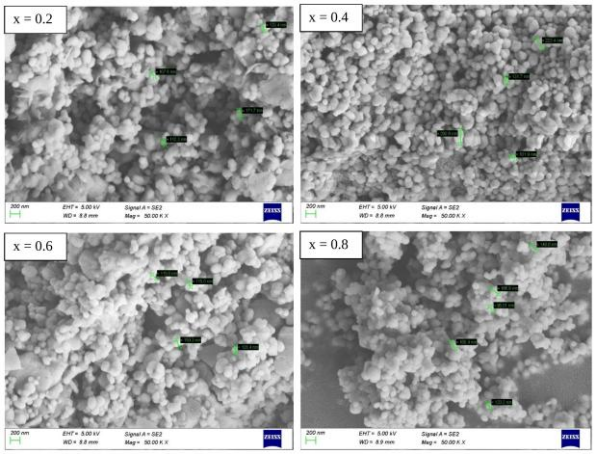


Fig.3 FESEM images of $Bi_{1-x}Ni_xFeO_3$ (x = 0.2 - 0.8) nanoparticles

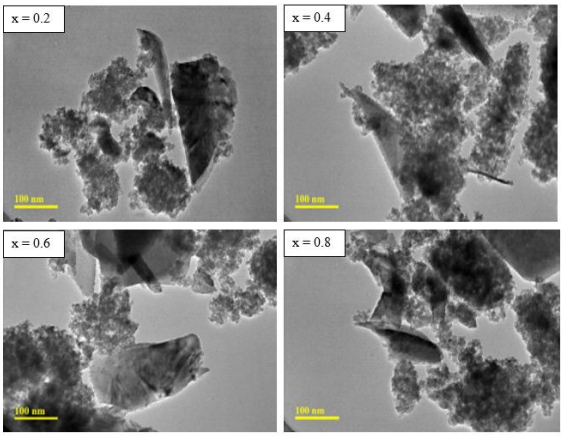


Fig.4 HRTEM patterns of $Bi_{1-x}Ni_xFeO_3$ (x = 0.2 - 0.8) nanoparticles

© JUL 2026 | IRE Journals | Volume 10 Issue 1 | ISSN: 2456-8880
DOI: https://doi.org/10.64388/ire1724954

B. FT-IR Analysis

The FTIR spectra exhibit several distinct absorption features over the investigated spectral range, demonstrating the presence of vibrational modes associated with the oxide nanoparticle lattice and surface-related groups. The prominent features occur in the high-wavenumber region around 3440–3520 cm^{-1}, in the 1600–1720 cm^{-1} region, around 1380–1485 cm^{-1}, near 1030–1075 cm^{-1}, and in the lower-wavenumber region. An absorption observed around 1651 cm^{-1} for the x = 0.2 – 0.8 compositions. This band can be associated primarily with the bending vibration of molecularly adsorbed water (H–O–H) and surface hydroxyl-related species. Its variation with Ni concentration suggests changes in the surface chemistry and defect concentration of the nanoparticles. The absorption band near1388 cm^{-1} may be related to vibrations involving surface hydroxyl groups and/or residual precursor-related species.

The FTIR spectra demonstrate that increasing the Ni concentration from x = 0.2 to 0.8 produces noticeable changes in the position, width, and intensity of the absorption bands. These changes can be attributed to the difference in the ionic radius, mass, and bonding characteristics of Ni^{2+} compared with Fe^{3+}. Since Ni^{2+} replaces Fe^{3+} in the $BiFeO_3$ lattice, charge compensation may occur through the development of oxygen vacancies and/or changes in the Fe^{2+}/Fe^{3+} ratio. Such modifications can alter the force constants and vibrational frequencies of the metal–oxygen bonds. The band observed near 1055 cm^{-1} is attributed to vibrational modes involving metal–oxygen bonding and surface-related oxygen species. Changes in this band with Ni concentration provide evidence that the incorporation of Ni^{2+} ions modify the local coordination environment of the Fe–O/Bi–O framework. The band near 769 cm^{-1} becomes particularly distinguishable in the higher-Ni compositions. This region is associated with lattice vibrational modes involving the metal–oxygen framework.

The FTIR results confirm that the synthesized $Bi_{1-x}Ni_xFeO_3$ nanoparticles contain characteristic vibrational modes associated with the oxide lattice and surface species. The gradual changes in the spectra also support the XRD observations that Ni incorporation affects the crystal structure and lattice parameters of $Bi_{1-x}Ni_xFeO_3$. Thus, FTIR provides complementary evidence for the successful modification of the $BiFeO_3$ lattice by Ni doping.

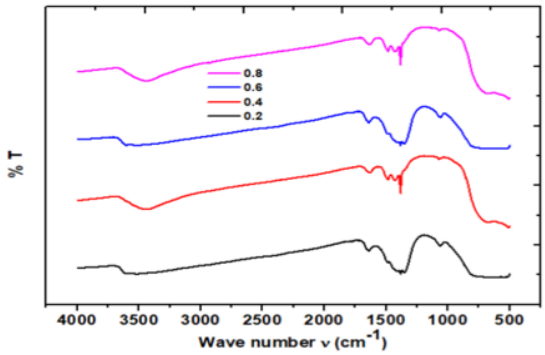


Fig.5 FTIR spectra of $Bi_{1-x}Ni_xFeO_3$ (x = 0.2 - 0.8) nanoparticles

C. UV–Visible Diffuse Reflectance Spectroscopy Analysis

UV–Vis–NIR spectroscopy was employed to investigate the optical properties and determine the optical band gap energy of $Ni_xBi_{1-x}FeO_3$ (BNF) nanoparticles. The function of reflectance

$$F(r) = 0.5\,\frac{(1-r)^2}{r}$$

or Kubelka-Munk function is calculated for the data received from UV-Visible spectral studies of BNF samples. The absorption coefficient (α) is calculated by considering the directly proportional relationship with function of reflectance. Therefore, the F(r) is taken as α, and furthermore, the Tauc plots are drawn as shown in figure 6. The plots are drawn between hυ versus $(\alpha h\upsilon)^2$ by following the equation:

$$(\alpha h\nu)^2 = A(h\nu - E_g)$$

where:

$\alpha \rightarrow$ absorption coefficient,

$h\nu \rightarrow$ photon energy,

$A \rightarrow$ *proportionality* constant, and

$E_g \rightarrow$ optical band gap energy.

That is, in the case of direct transition, exponent n equals to 2 while the direct forbidden reveals n = 2/3, and the indirect transitions express n = 1/2 [26-27]. In the case of BNF, the n-value for direct transition is taken into an account. In the Tauc plots, it is seen that the linear portion is extrapolated towards the $h\nu -$ *axis*. The intersecting point of the axis demonstrates the E_g value. At this point, the absorption coefficient lasts as null, wherein, the optical bandgap is possible to measure. The estimated optical band gap values are presented in Table 2.

© JUL 2026 | IRE Journals | Volume 10 Issue 1 | ISSN: 2456-8880
DOI: https://doi.org/10.64388/ire1724954

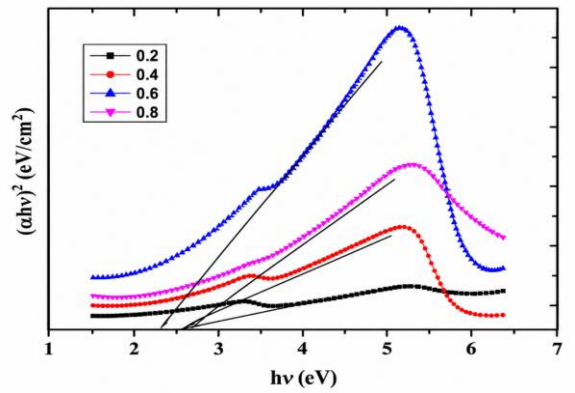


Fig.6 Tauc plots of $Bi_{1-x}Ni_xFeO_3$ (x = 0.2–0.8) nanoparticles.

Table 2: Optical band gap energy of $Bi_{1-x}Ni_xFeO_3$ nanoparticles

Ni Concentration 'x'	E_g (eV)
0.2	2.7
0.4	2.6
0.6	2.3
0.8	2.5

The results reveal a gradual reduction in the E_g value from 2.7 eV to 2.3 eV with increasing Ni concentration up to x = 0.6. However, a slight increase to 2.5 eV is observed at x = 0.8. The reduction in band gap may be attributed to structural distortion, changes in Fe–O bond interactions, and the formation of defect states associated with Ni substitution. These modifications influence the electronic structure and facilitate electronic transitions at lower photon energies. The increase in band gap at x = 0.8 may be associated with changes in oxygen vacancy concentration and the resulting electronic structure [26].

The linear region of the graph indicates the onset of strong optical absorption resulting from electronic transitions between the valence band and conduction band. Extrapolation of this region to $(\alpha h\upsilon)^2 = 0$ yields the direct band gap energy. From the graph, the extrapolated intercepts indicate band gap values, and they show a clear reduction in optical band gap with increasing dopant concentration.

Among the investigated compositions, the sample with x = 0.6 exhibits the lowest optical band gap of approximately 2.3 eV, indicating improved absorption in the visible-light region. This behaviour suggests that Ni substitution provides an effective means of tuning the optical properties of $BiFeO_3$ nanoparticles.

The observed band gap modification is important for potential applications in visible-light-driven photocatalysis, solar energy conversion, optical sensors, photodetectors and optoelectronic devices. In particular, the reduced band gap may promote light absorption and electronic excitation, making Ni-doped $BiFeO_3$ nanoparticles promising materials for optical and energy-related applications. Furthermore, enhanced visible-light absorption can improve charge-carrier generation and increase photocatalytic efficiency by utilizing a larger fraction of the solar spectrum.

D. Magnetic Properties of BiNiFeO3 Nanoparticles by M-H Curve Analysis:

The magnetic field-dependent magnetization (M-H) curves of BNF samples with nickel concentration (x = 0.2 - 0.8) were examined over an applied magnetic field range of approximately -15K to +15K Oe. The curves exhibit nonlinear, S-shaped behaviour with hysteresis-like central branches, indicating a field-dependent magnetic response shown I figure 7.

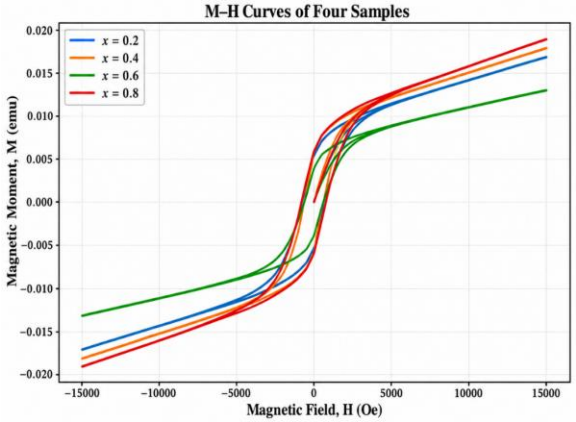


Fig.7 The M-H curves of $Bi_{1-x}Ni_xFeO_3$ (x = 0.2 - 0.8) nanoparticles

The results show that the magnetic response of $BiFeO_3$ is strongly influenced by Ni substitution. The saturation magnetisation M_s increases slightly from 16.889×10^{-3} emu for x = 0.2 to 17.899×10^{-3} emu for x = 0.4, followed by a decrease to 12.989×10^{-3} emu at x = 0.6. A pronounced increase is observed at x = 0.8, where the highest M_s of 18.855×10^{-3} emu is obtained as in table 3. A similar variation is observed in M_r, with the maximum value of 5.948×10^{-3} emu occurring for x = 0.8. It is seen that the individual magnetic moment values of cations present in the system can be noted as Ni^{2+}:2.2 μB, Fe^{3+}: 5.29 μB, Fe^{2+}:4.9 μB, and Bi^{3+}: 3 μB as reported in the literature [28-30]. Upon doping the Ni content into the multiferroic perovskite BF, the general probability for the magnetization is reduction as it can replace the ferric ions. Moreover, the possible occupancy for the Ni^{2+}, Fe^{3+} & Fe^{2+} can be considered as both A & B-sites in the ABO_3 structure. But the cations present at the B-site can actually induce the magnetization. This depends on the cationic distribution. That is, once the Ni-cations are doped, the ferric ions of high magnetic moment will be migrated from B-site to A-site. Sometimes, the similar ions may prefer the A-site replacing the ferric ions, and therefore, the chances are

very high to obtain high magnetization thereby achieving the high magnetic moment. Due to this reason, the M_s values are not varying monotonically with increase in Ni-content. From this analysis, it is an established fact that the x = 0.2, 0.4 & 0.8 pertain the Ni-cationic occupancy as A-site while the x = 0.6 shows the probable Ni-cationic occupancy as B-site, and that is why, the high magnetization (where magnetic exchange interactions between Fe-O-Fe can be high) is found for the same while low value is recorded for x = 0.6 (where magnetic exchange interactions between Fe-O-Fe can be reduced a little). The similar type of discussion is given in the literature [28-30].

Table 3. The magnetization values of $Bi_{1-x}Ni_xFeO_3$ (x = 0.2 - 0.8) nanoparticles extracted from the M–H plot

Sample	Ms (emu)	Mr (emu)	Hci (Oe)	Mr/Ms
x = 0.2	16.889×10^{-3}	5.337×10^{-3}	722.45	0.316
x = 0.4	17.899×10^{-3}	5.705×10^{-3}	599.44	0.319
x = 0.6	12.989×10^{-3}	3.958×10^{-3}	606.38	0.305
x = 0.8	18.855×10^{-3}	5.948×10^{-3}	765.71	0.315

The coercive field varies between 599.44 and 765.71 Oe. The lowest Hc is observed for x = 0.4 (599.44 Oe), while the highest value occurs for x = 0.8 (765.71 Oe). The relatively high coercive fields indicate appreciable resistance to magnetization reversal and suggest enhanced hard-magnetic characteristics at higher Ni concentration wherein; the paramagnetic term is present. The increase in coercivity at x = 0.8 may be associated with changes in magnetic anisotropy, particle size, defect concentration, and exchange interactions resulting from Ni substitution.

The observed non-linear variation of M_s and M_r with Ni concentration suggests that Ni^{2+} substitution modifies the magnetic exchange interactions within the $BiFeO_3$ lattice. In pure $BiFeO_3$, the antiferromagnetic spin structure generally results in weak net magnetization. Substitution by Ni^{2+} can disturb the Fe–O–Fe superexchange interaction and introduce spin canting, thereby producing a measurable ferromagnetic component. The reduction in magnetization at x = 0.6 may indicate increased magnetic disorder or competing exchange interactions, whereas the subsequent enhancement at x = 0.8 suggests stronger uncompensated/canted magnetic moments.

The Mr/Ms ratio is approximately 0.316, 0.319, 0.305 and 0.315 for x = 0.2, 0.4, 0.6 and 0.8, respectively. Since all values are considerably below 0.5, the samples exhibit characteristics consistent with predominantly soft-to-intermediate magnetic behaviour, despite their relatively high coercive fields. Overall, the magnetic measurements demonstrate that Ni doping provides an effective means of tailoring the magnetic properties of $BiFeO_3$ nanoparticles, with the x = 0.8 composition exhibiting the highest saturation and remanent magnetization as well as the highest coercivity among the investigated samples.

E. Thermal Analysis of BiNiFeO3 Nanoparticles Using TG-DSC Techniques

Thermogravimetric (TG) and Differential Scanning Calorimetry (DSC) analyses were carried out to investigate the thermal stability, weight-loss (Δm) behaviour and thermal transitions of nickel-doped bismuth ferrite ($BiNiFeO_3$) nanoparticles [31-35]. Figure 8 shows the thermogravimetric (TG) analysis as a function of temperature of BNFO. The TG curves reveal the variation in sample weight with temperature, whereas the DSC curves provide information about thermal events and associated enthalpy changes. These studies help to understand the thermal behaviour and stability of the synthesized nanoparticles.

In the TG curves, it conveys that the x = 0.2 shows the considerable weight loss at two temperatures ~232.5 & 638.3°C possessing 7 & 18 %, respectively. The x = 0.4 reveals the 9 & 21 % of weight loss at 265.2 & 655.4°C, respectively. The x = 0.6 offers almost similar kind of weight loss values at 250.8 & 610.3°C temperatures. Finally, the x = 0.8 provides the 11 & 18 % of Δm values at 270.5 & 640.7°C, respectively. As a whole, analysis confirm the high weight loss values for x = 0.4 & 0.6 samples. This can be attributed to the drastic loss of moisture and other ingredient species present in the BNFO nanoparticles with increase in temperature [36-40]. Normally, the x = 0.2 - 0.8 samples indicate the removal of moisture, nitrate materials and others at the temperatures between 232.5-270.5°C. The other high temperatures indicate the formation of BNFO compound or in other words, it is called as the crystallization process. All four samples exhibit relatively stable behaviour at temperatures above approximately 650 °C.

© JUL 2026 | IRE Journals | Volume 10 Issue 1 | ISSN: 2456-8880
DOI: https://doi.org/10.64388/ire1724954

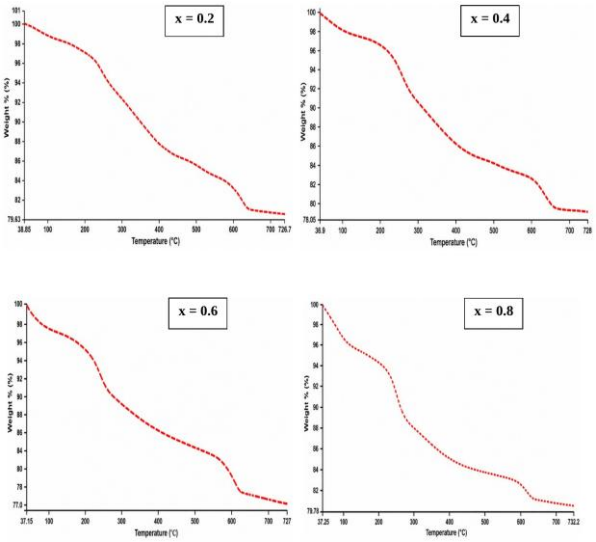


Fig. 8 The TG curves of $Bi_{1-x}Ni_xFeO_3$ (x = 0.2-0.8) nanoparticles

Furthermore, the DSC curves are shown in figure 9**.** The DSC curves exhibit two prominent thermal events for each sample, indicating different thermal transitions during heating. The corresponding peak temperatures and enthalpy values are summarized below. They reveal that the peak temperatures of x = 0.2 - 0.8 as 354.1, 274.2, 269.3 & 257.5°C and 716.5, 602.2, 603.1 & 560.2°C. The first peak position temperatures establish the glass transition temperatures while the rest temperatures show the crystallization temperatures, where the process of forming the crystallite, and further forming the BNFO compound takes place [41-45]. The variation in peak temperatures and enthalpy values indicates that nickel concentration may influence the thermal behaviour of the synthesized nanoparticles.

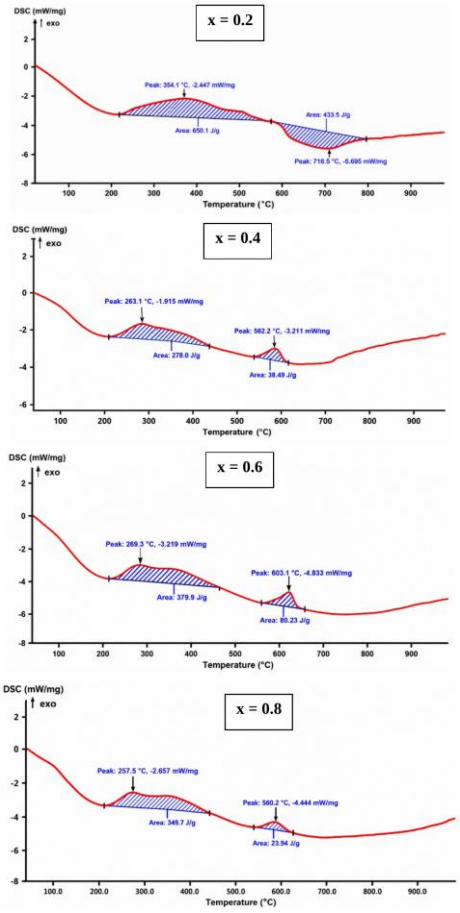


Fig.9 The DSC curves of $Bi_{1-x}Ni_xFeO_3$ (x = 0.2 - 0.8) nanoparticles

The TG and DSC analyses demonstrate that nickel-doped $BiFeO_3$ nanoparticles exhibit multistage thermal behaviour during heating. The DSC curves reveal two major thermal events, with the first occurring between 257.5 and 354.1 °C and the second between 560.2 and 716.5 °C. Variations in peak temperatures and enthalpy values indicate differences in the thermal response of the samples with nickel doping. Overall, the results suggest that the synthesized nickel-doped $BiFeO_3$ nanoparticles possess good thermal stability at elevated temperatures.

IV. CONCLUSION

In the present investigation, Ni-doped bismuth ferrite ($Bi_{1-x}Ni_xFeO_3$, x = 0.2, 0.4, 0.6 and 0.8) nanoparticles were successfully synthesized using the hydrothermal method, and their structural, morphological, optical, magnetic and thermal properties were systematically investigated. The X-ray diffraction results confirmed the formation of a predominantly rhombohedral $BiFeO_3$-based crystalline structure, accompanied by minor secondary phases corresponding to $Bi_2Fe_4O_9$. The systematic

variations in lattice parameters and unit cell volume indicate structural modifications associated with Ni^{2+} incorporation into the $BiFeO_3$ lattice. The crystallite size varied from 45.5 to 69.1 nm, demonstrating the influence of Ni concentration on crystallite growth and structural ordering. FESEM and HRTEM analyses further revealed nanoscale particle formation with relatively homogeneous morphology. The FTIR spectra exhibited characteristic vibrational bands associated with metal–oxygen bonding and surface functional groups, providing additional evidence of changes in the local bonding environment due to Ni substitution.

The optical studies revealed a significant compositional dependence of the optical band gap, decreasing from 2.7 eV for x = 0.2 to 2.3 eV for x = 0.6, followed by a slight increase to 2.5 eV for x = 0.8. The minimum band gap observed for the x = 0.6 composition indicates enhanced visible-light absorption, suggesting its potential suitability for optical and energy-related applications. The magnetic measurements demonstrated a non-monotonic variation in saturation magnetization and remanent magnetization with increasing Ni concentration. Among the investigated compositions, the x = 0.8 sample exhibited the highest saturation magnetization (18.855×10^{-3} emu), remanent magnetization (5.948×10^{-3} emu) and coercivity (765.71 Oe). These variations can be associated with modifications in Fe–O–Fe superexchange interactions, spin canting, magnetic disorder and changes in the cationic environment induced by Ni substitution. The relatively low squareness ratios (0.305–0.319) further indicate predominantly soft-to-intermediate magnetic characteristics.

Furthermore, TG–DSC analysis revealed multistage thermal behaviour, with initial weight losses associated with the removal of moisture and residual precursor species, followed by higher-temperature thermal transitions associated with crystallization and oxide-phase development. The DSC results exhibited two major thermal events, with peak temperatures ranging from 257.5 to 354.1 °C and 560.2 to 716.5 °C, respectively. The observed thermal behaviour indicates composition-dependent thermal transitions and comparatively stable characteristics at elevated temperatures.

Overall, the present findings establish that Ni substitution is an effective strategy for tailoring the structural, optical, magnetic and thermal properties of $BiFeO_3$ nanoparticles synthesized through the hydrothermal route. Notably, the x = 0.6 composition exhibits the lowest optical band gap, whereas the x = 0.8 composition demonstrates the superior magnetic response among the investigated samples. These results highlight the importance of Ni concentration in optimizing the multifunctional characteristics of $BiFeO_3$-based nanomaterials and indicate their potential for future applications in magnetic, spintronic, optoelectronic and visible-light-related devices. Further investigations involving detailed cation distribution, phase-purity optimization and electrical and ferroelectric characterization would provide deeper insight into their multifunctional performance and practical applicability.

REFERENCES

[1] Mitzi, D.B. Introduction: Perovskites. *Chemical Reviews* 2019, 119(5), 3033–3035. https://doi.org/10.1021/acs.chemrev.8b00800

[2] Liu, H.; Yang, X. A brief review on perovskite multiferroics. *Ferroelectrics* 2017, 507(1), 69–85. https://doi.org/10.1080/00150193.2017.1283171

[3] Korde, V.B.; Khot, S.; Kamble, D.B.; et al. Review: Perovskite nanostructures materials versatile platform for advance biosensor applications. *Sensors and Actuators Reports* 2024, 7, 100201. https://doi.org/10.1016/j.snr.2024.100201

[4] Yin, Y.; Li, Q. A review on all-perovskite multiferroic tunnel junctions. *Journal of Materiomics*. 2017, 3(4), 245–254. https://doi.org/10.1016/j.jmat.2017.09.001

[5] Suresh, K. N.; Chandra, B.N.K. A review on perovskite solar cells (PSCs), *materials and applications. Journal of Materiomics* 2021, 7(5), 940–956. https://doi.org/10.1016/j.jmat.2021.04.002

[6] Mujtaba, A.; Khan, M.I.; Nadeem, M.A.; et al. Green hydrothermal synthesis of Mg-doped transition metal dichalcogenides using *Camellia sinensis* extract for enhanced energy storage. *Journal of Sol-Gel Science and Technology* 2025, 115, 457–470. https://doi.org/10.1007/s10971-025-06818-1

[7] Nanostructured Multiferroics. Wiley; 2012. pp. 233–247. https://doi.org/10.1002/9783527809967.ch9

[8] Carranza-Celis, D.; Cardona-Rodríguez, A.; Narváez, J.; et al. Control of Multiferroic properties in BiFeO3 nanoparticles. Scientific Reports 2019, 9, 3182. https://doi.org/10.1038/s41598-019-39517-3

[9] Indriyani, A.; Yulizar, Y.; Tri, Y.R.; et al. One-pot green fabrication of BiFeO3nanoparticles via Abelmoschus esculentus L. le aves extracts for photocatalytic dye degradation. Applied Surface Science 2021, 563, 150113. https://doi.org/10.1016/j.apsusc.2021.150113

[10] Amdouni, W.; Fricaudet, M.; Otoničar, M.; et al. BiFeO3 Nanoparticles: The "Holy-Grail" of Piezo Photocatalysts? Advanced Materials 2023, 35(31), 2301841. https://doi.org/10.1002/adma.202301841

[11] Basith, M.A.; Yesmin, N.; Hossain, R. Low temperature synthesis of BiFeO3 nanoparticles with enhanced magnetization and promising photocatalytic performance in dye degradation and hydrogen evolution. RSC Advances 2018, 8(52), 29613–29627. https://doi.org/10.1039/c8ra04599b

[12] Bai, X.; Bugnet, M.; Frontera, C.; et al. Crystal Growth Mechanisms of BiFeO3 Nanoparticles. Inorganic Chemistry 2019, 58(17), 11364–11371. https://doi.org/10.1021/acs.inorgchem.9b00461

[13] Mocherla, P.S.V.; Karthik, C.; Ubic, R.; et al. Tunable bandgap in BiFeO3 nanoparticles: The role of microstrain

and oxygen defects. *Applied Physics* Letters 2013, 103(2), 022910. https://doi.org/10.1063/1.4813539

[14] Prince, M.H.; Aishi, T.M.; Zubair, Md. A.; et al. Tuning of the Structural, Optical and Magnetic Properties of BiFeO3 Nanoparticles by Annealing. In: *Tuning of the Structural, Optical and Magnetic Properties of BiFeO3 Nanoparticles by Annealing*, Proceedings of the 2023 IEEE International Conference on Telecommunications and Photonics (ICTP); 21–23 December 2023, Dhaka, Bangladesh. IEEE; 2023, pp. 01–05. https://doi.org/10.1109/ictp60248.2023.10490725

[15] Masoudpanah, S.M.; Mirkazemi, S.M. *Journal of Nanostructures* 2017, 7(3), 183–188. https://doi.org/10.22052/jns.2017.03.003

[16] Othman, M.; Mallek-Zouari, I.; Akrout, H.; et al. Synthesis and properties of ultra-small BiFeO3 nanoparticles doped with cobalt. *Ceramics International* 2023, 49(7), 10580–10587. https://doi.org/10.1016/j.ceramint.2022.11.245

[17] Shrimali, V.G.; Rathod, K.N.; Dhruv, D.; et al. Magnetoelectric properties of Co-doped BiFeO3 nanoparticles. International Journal of Modern Physics B 2018, 32(12), 1850143. https://doi.org/10.1142/s0217979218501436

[18] Gu, Y.; Zhou, Y.; Zhang, W.; et al. Optical and magnetic properties of Sm-doped BiFeO3 nanoparticles around the morphotropic phase boundary region. AIP Advances 2021, 11(4), 045223. https://doi.org/10.1063/5.0042485

[19] Shameem, B.I.B.; Divya, L.S.; Kossar, S.; et al. Substitution driven optical and magnetic properties of neodymium and nickel doped BiFeO3 ceramics for spintronics applications. In Proceedings of the 2018 International Conference on Recent Trends in Electrical, Control and Communication (RTECC); 20–22 March 2018; Malaysia, Malaysia. pp. 93–98. https://doi.org/10.1109/rtecc.2018.8625635

[20] Sarkar, K.; Mukherjee, S.; Mukherjee, S. Structural, electrical and magnetic behaviour of undoped and nickel doped nanocrystalline bismuth ferrite by solution combustion route. Processing and Application of Ceramics 2015, 9(1), 53–60. https://doi.org/10.2298/pac1501053s

[21] Mallikarjuna, A.; Ramesh, S.; Suresh, K.N.; et al. Structural transformation and high nega tive dielectric constant behavior in (1-x) (Al0·2La0·8TiO3) + (x) (BiFeO3) (x = 0.2–0.8) nanocomposites. *Physica E: Low dimensional Systems and Nanostructures* 2020,122, 114204. https://doi.org/10.1016/j.physe.2020.114204

[22] Venkata, S.R.B.; Srinivas, K.; Suresh K.N.; et al. Nanorods like microstructure, photocatalytic activity and ac-electrical properties of (1-x) (Al0.2La0.8TiO3) + (x) (BaTiO3) (x = 0.2, 0.4, 0.6 & 0.8) nanocomposites. *Chemical Physics* Letters 2020, 752, 137552. https://doi.org/10.1016/j.cplett.2020.137552

[23] Sahu, S.; Mohapatra, P.P.; Karnajit Singh, H.; et al. Enhanced microwave absorbing performance of Sr2+substituted Nickel-Cobalt nano ferrite for radar and stealth applications. *Materials Science and Engineering*: B 2023, 294, 116514. https://doi.org/10.1016/j.mseb.2023.116514

[24] Shannon, R.D. Revised effective ionic radii and systematic studies of interatomic distances in halides and chalcogenides. *Acta Crystallographica Section A 1976, 32, 751–767.* https://doi.org/10.1107/s0567739476001551

[25] Nadeem, M.; Khan, W.; Khan, S.; et al. Significant enhancement in photocatalytic performance of Ni doped BiFeO3 nanoparticles. *Materials Research Express 2018, 5(6), 065506.* https://doi.org/10.1088/2053-1591/aac70d

[26] Kumar, N.S.; Suvarna, R.P.; Naidu, K.C.B. Sol-gel synthesized and microwave heated $Pb_{0.8-y}La_yCo_{0.2}TiO_3$ (y = 0.2–0.8) nanoparticles: Structural, morphological and dielectric properties. Ceramics International 2018, 44(15), 18189–18199. https://doi.org/10.1016/j.ceramint.2018.07.027

[27] Dastagiri, S.; Lakshmaiah, M.V.; Chandra, B.N.K. Defect dipole polarization mechanism in low dimensional europium substituted $Al_{0.8}La_{0.2}TiO_3$ nanostructures. Physica E: Low-dimensional Systems and Nanostructures 2020, 120, 114058. https://doi.org/10.1016/j.physe.2020.114058

[28] Mukherjee, A.; Basu, S.; Manna, P.K.; Yusuf, S.M.; Pal, M. Enhancement of multiferroic properties of nanocrystalline BiFeO3 powder by Gd-doping. J. Alloys Compd. 2014, 598, 142-50, https://doi.org/10.1016/j.jallcom.2014.01.245.

[29] Ablat, A.; Wu, R.; Mamat, M.; Li, J.; Muhemmed, E.; Si, C.; Wu, R.; Wang, J.; Qian, H.; Ibrahim, K. Structural analysis and magnetic properties of Gd doped BiFeO3 ceramics. Ceram. Int. 2014, 40, 14083-14089, https://doi.org/10.1016/j.ceramint.2014.05.137.

[30] Suresh, P.; Babu, P.D.; Srinath, S. Role of (La, Gd) co-doping on the enhanced dielectric and magnetic properties of BiFeO3 ceramics. Ceram. Int. 2016, 42, 4176-4184, https://doi.org/10.1016/j.ceramint.2015.11.091.

[31] Kumari, P. A., Devi, D. M., Chandrasekhar, M., & Kumar, N. S. V. (2025). Structure, Dielectric, and Thermal Behavior of Bismuth Titanate Nanoparticles. Chemistry Select, 10(5). https://doi.org/10.1002/slct.202404134

[32] Rajender, T., Naidu, K. C. B., et al. (2024). Magnetic, dielectric and thermal study of $CoNiFe_2O_4$ nanoparticles. In Nano-Structures & Nano-Objects (Vol. 38, p. 101167). Elsevier BV. https://doi.org/10.1016/j.nanoso.2024.101167

[33] Jin, Z., Zhang, G., Gao, W., Jiang, H., Li, G., & Geng, X. (2025). Ignition and combustion mechanisms in Mg-Al alloys via TG-DSC and Reax FFMD simulations. Advanced Powder Technology, 36(11), 105062. https://doi.org/10.1016/j.apt.2025.105062

[34] Zhou, R.-B., Zhao, J.-J., Ren, N., Zhang, Z.-H., & Zhang, J.-J. (2026). Synergistic thermal and luminescence investigation of dinuclear RE(III) complexes with fluorinated ligands: Combined TG-DSC/FTIR/MS analysis. Journal of Molecular Structure, 1358, 145358. https://doi.org/10.1016/j.molstruc.2026.145358

[35] Liu, J., Liu, Z., Zhu, J., Zhang, G., Li, Y., Sun, Z., Zhou, H., Zhou, Z., Deng, X., & Liu, Y. (2025). Study on thermal decomposition and combustion mechanism of azobisisobutyronitrile: Combined with TG-DSC-FTIR-GC-MS technology and the ReaxFF molecular dynamics. Chemical Physics, 599, 112880. https://doi.org/10.1016/j.chemphys.2025.112880

[36] Yao, H., Xiong, Y., Koskela, A., Fabritius, T., & Omran, M. (2026). Pyrolysis behaviour of different biomass by-products generated in Finland: Kinetics study and FTIR-DSC, TG-MS characterisation. Thermochimica Acta, 756, 180208. https://doi.org/10.1016/j.tca.2025.180208

[37] Lei, J., Zhang, Y., Zhou, J., Deng, S., & Fu, Y. (2026). Study of the combustion behavior of wheat straw using TG–DSC under multiple heating rates. Biomass and Bioenergy, 205, 108507. https://doi.org/10.1016/j.biombioe.2025.108507

[38] Chen, Y., Tan, H., Yan, M., Li, Y., You, X., Yin, H., He, D., & Gong, H. (2024). Updated understandings on coke formation during the inferior heavy oil in-situ combustion process: A combined FTIR, XPS, TG/DTG, and DSC

study. Sustainable Energy Technologies and Assessments, 65, 103772. https://doi.org/10.1016/j.seta.2024.103772

[39] Wang, L., Wang, T., Zhang, Y., Peng, X., Song, W., Yang, J., & Yuan, C. (2023). Oxidation behaviors of Hongqian heavy crude oil characterized by TG-DSC-FTIR-MS within full temperature regions. Fuel, 353, 129242. https://doi.org/10.1016/j.fuel.2023.129242

[40] Du, J., Dou, B., Zhang, H., Wu, K., Gao, D., Wang, Y., Chen, H., & Xu, Y. (2023). Non-isothermal kinetics of biomass waste pyrolysis by TG-MS/DSC. Carbon Capture Science & Technology, 6, 100097. https://doi.org/10.1016/j.ccst.2023.100097

[41] Liu, S.-H., & Xia, R. (2023). Evaluation of the thermal stability and pyrolysis mechanism of 1-ethyl-3-methylimidazolium dicyanamide and 1-Butyl-3-methylimidazolium dicyanamide by STA, DSC, TG-FTIR. Journal of Loss Prevention in the Process Industries, 85, 105153. https://doi.org/10.1016/j.jlp.2023.105153

[42] Salehi, S., Eslami, A., Chu, Q., & Chen, D. (2024). Superb enhancement of thermal decomposition of ammonium perchlorate in the presence of methyl viologen salts: A TG-DSC/MS and kinetic study. Journal of Analytical and Applied Pyrolysis, 178, 106415. https://doi.org/10.1016/j.jaap.2024.106415

[43] Rico, J. J., Pérez-Orozco, R., Patiño Vilas, D., & Porteiro, J. (2022). TG/DSC and kinetic parametrization of the combustion of agricultural and forestry residues. Biomass and Bioenergy, 162, 106485. https://doi.org/10.1016/j.biombioe.2022.106485

[44] Teixeira, J. A., Fernandes, R. P., Isquibola, G., Gaspari, A. P. S., Machado, A. E. H., Caires, F. J., & Ionashiro, M. (2022). Synthesis, thermal behavior in oxidative and pyrolysis conditions, spectroscopic and DFT studies of some alkaline earth metals p-aminobenzoate complexes using TG-DTA, DSC, PXRD and EGA (TG-FTIR) techniques. Thermochimica Acta, 711, 179184. https://doi.org/10.1016/j.tca.2022.179184

[45] Sebestyén, Z., Badea, E., Carsote, C., Czégény, Z., Szabó, T., Babinszki, B., Bozi, J., & Jakab, E. (2022). Characterization of historical leather bookbindings by various thermal methods (TG/MS, Py-GC/MS, and micro-DSC) and FTIR-ATR spectroscopy. Journal of Analytical and Applied Pyrolysis, 162, 105428. https://doi.org/10.1016/j.jaap.2021.105428